Radio Tomography Imaging using Adjacent Criterion Method to determine the Localization Error

M. S. M. Abdullah[†], **M. H. F. Rahiman**, **Nurul Syahirah Binti Khalid**, **Aimi Salihah Abdul Nasir**, and **N. A. Ramli**, Non-members

ABSTRACT

Observed that most setup have limitations in the number of Radio Frequency (RF) nodes due to a limited number of measurements. However, it is well known that the main difficulty in radio tomographic imaging attributes to the uncertainties in the Receive Signal Strength (RSS) measurements of transceivers due to multipath effects especially, when the environment of interest is much cluttered, and requirements on the larger number of nodes for the performance improvements. However, no study has been conducted to solve the inverse problem and improve the quality of the reconstructed image using a reduced sensor model for Radio tomography system localization. This work focuses on the design and development of a Radio tomography system for human localization that will employ a transceiver sensor arrangement to increase the number of measurements, without making any changes to the hardware design as well as the number of pixels in the sensing domain. An image reconstruction technique namely Adjacent Criterion Method (ACM) was proposed to enhance the image spatial resolution. A number of experiments were used to evaluate the performance of the system. The results showed that the proposed technique improves the spatial resolution and exhibits more accurate tomograms.

Keywords: Adjacent Criterion Method, Image Reconstruction, Reduced Sensor Node

1. INTRODUCTION

Most of the researches presented in the area of RTI have focused on single target localization and tracking. However, in real-world indoor and outdoor contexts, RTI systems frequently require the localization and tracking of several objects with overlapping trajectories. As a result, several ongoing investigations are being carried out to improve the performance of the RTI system in terms of multitarget localization and accuracy, all studies used more than 20 RF sensor nodes [1-11], so in this work, have reduced the sensor node to 8 RF sensor nodes, considered the lowest number of sensor has been used in RTI research area. The 8 RT sensor nodes able to cover monitoring area for multitarget localization. The fundamental of RTI when increasing the number of the sensor will also increase the processing time. The motivation of using fewer nodes in this work is to reduce the deployment cost of radio tomographic imaging, faster data collection rates, shorter imaging reconstruction times, and smaller sensitivity matrices. An image reconstruction technique namely Adjacent Criterion Method (ACM) was proposed to enhance the image spatial resolution. ACM approach integrate with Linear Back- Projection (LBP), Filtered Back Projection (FBP)[12], Gaussian, Newton's One-step's Error Reconstruction (NOSER) and Tikhonov Regularization (TR) technique for improving the spatial resolution using the similar number of RT sensor node and without making any changes on the hardware. The method is discussed in the ACM section. In the proposed method, each projection was divided into two paths. When transmission occurs, the receiving sensors respond in accordance with ACM truth rules [12].

The localization and tracking of many targets are a difficulty in the Radio tomography imaging (RTI) system [13]. While shadowing caused by many targets is more difficult to model mathematically than shadowing caused by a single target, the majority of research is focused on a number of different targets. Localization assumes that the observed RSS variation is just the superimposition of that of a single target, necessitating the use of algorithms to identify them. In RTI system, one of the important challenges is investigate at how the correlated impact of multiple targets is represented in multiple antennae's RF measurements, and how to accomplish RTI localization accuracy with multiple targets utilizing a minor path difference produce by spatial diversity.

2. SEQUENTIAL PROCESSING

Tracking position is more easily accomplished when measurements are made at the same time. Once RSS readings from all transceivers are available at the base station, the processed using the RTI graphical

---

Manuscript received on May 8, 2023; revised on April 5, 2024; accepted on April 6, 2024. This paper was recommended by Associate Editor Kampol Woradit.

The authors are with Faculty of Electrical Engineering, Universiti Malaysia Perlis (UniMAP), Perlis, Malaysia.

[†] Corresponding author: mohammedsaeed188@gmail.com

Digital Object Identifier: 10.37936/ecti-eec.2024222.249427

$$TR = \begin{bmatrix} TR1 \\ TR2 \\ TR3 \\ TR4 \\ TR5 \\ TR6 \\ TR7 \\ TR8 \end{bmatrix} = \begin{bmatrix} 0 & TR1_{1,2} & TR1_{1,3} & TR1_{1,4} & TR1_{1,5} & TR1_{1,6} & TR1_{1,7} & TR1_{1,8} \\ TR2_{2,1} & 0 & TR2_{2,3} & TR2_{2,4} & TR2_{2,5} & TR2_{2,6} & TR2_{2,7} & TR2_{2,8} \\ TR3_{3,1} & TR3_{3,2} & 0 & TR3_{3,4} & TR3_{3,5} & TR3_{3,6} & TR3_{3,7} & TR3_{3,8} \\ TR4_{4,1} & TR4_{4,2} & TR4_{4,3} & 0 & TR4_{4,5} & TR4_{4,6} & TR4_{4,7} & TR4_{4,8} \\ TR5_{5,1} & TR5_{5,2} & TR5_{5,3} & TR5_{5,4} & 0 & TR5_{5,6} & TR5_{5,7} & TR5_{5,8} \\ TR6_{6,1} & TR6_{6,2} & TR6_{6,3} & TR6_{6,4} & TR6_{6,5} & 0 & TR6_{6,7} & TR6_{6,8} \\ TR7_{7,1} & TR7_{7,2} & TR7_{7,3} & TR7_{7,4} & TR7_{7,5} & TR7_{7,6} & 0 & TR7_{7,8} \\ TR8_{8,1} & TR8_{8,2} & TR8_{8,3} & TR8_{8,4} & TR8_{8,5} & TR8_{8,6} & TR8_{8,7} & 0 \end{bmatrix} \quad (1)$$

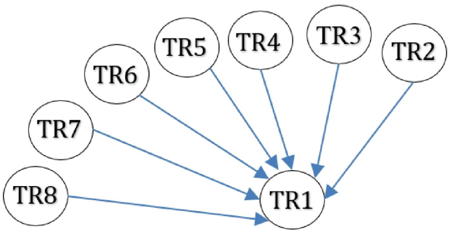

TR1= $[0 \ TR1_{1,2} \ TR1_{1,3} \ TR1_{1,4} \ TR1_{1,5} \ TR1_{1,6} TR1_{1,7} \ TR1_{1,8}]$

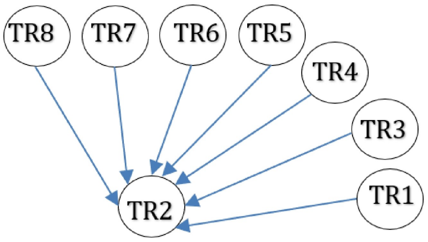

TR2= $[TR2_{2,1} \ 0 \ TR2_{2,3} \ TR2_{2,4} \ TR2_{2,5} \ TR2_{2,6} TR2_{2,7} \ TR2_{2,8}]$

***Fig. 1**: Example transmitter reports for the first communication node TR1 through TR8 reports are used to create a measuring matrix.*

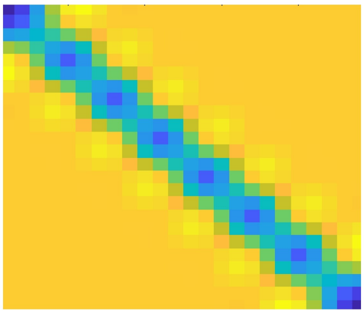

***Fig. 2**: A wireless network connection in a LOS direction.*

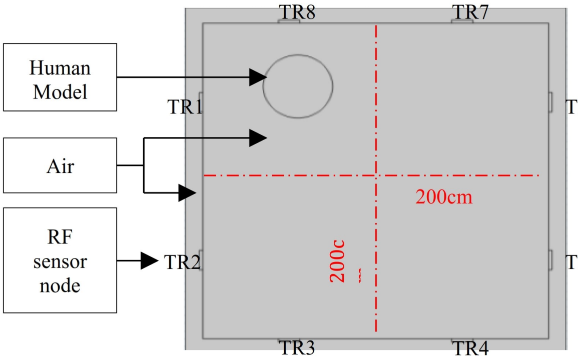

***Fig. 3**: Configuration of RTI system of 8 RF nodes.*

user interface. Another method for processing RSS measurements is to divide vectorizing the measurement matrix that represent RSS measurements made at the same time instant [1]. An essential difference should be established so that the measuring time (the RSS on a certain connection) is taken does not coincide with the time it is published. RSS readings obtained at various periods are included in each report in an RTI wire sensor network (WSN) [2]. The matrix of measurement Z is designed so that the RSS from transmitter j to receiver i is represented by the element Z(i,j). Using an eight-node RTI system to demonstrate how it works.

The measurement matrix in (1) assumes that one round of data has already been acquired from the whole WSN. Fig. 2 depicts the construction of the measuring matrix.

N sensor nodes are scattered throughout the monitoring region. Any two sensor nodes can build a line of sight (LOS) path, and the total number of linkages is indicated by Z=N(N-1)/2. N voxels are used to partition the monitoring region. The RSS value is modified when a target enters the monitoring region[3].Although attenuation occurs only at pixels in the LOS route, the weight of pixels that are not in the LOS line should be zero. Fig. 2 depicts a wireless network link that is a LOS route. The transmitting and receiving nodes are in the ellipse's center [4]. The matching weight is 1 when the pixel is included within the ellipse; otherwise, the weight is 0.

3. CONFIGURATION OF RTI SETUP

Fig. 3 depicts the configuration under consideration in this work. Each RF node was encapsulated and placed at an identical distance apart. They were set up in such a way that they received the scattered field from several directions, resulting in a slice of images. To explore the human, the simulation setting was used. The system was designed based on RF sensor nodes with a frequency of 2.4 GHz and air medium. The system has 8 RF sensor nodes as shown in Fig. 3, between each node 66.6 cm, monitoring area 200 cm x 200 cm.

***Table 1**: List of parameters for RTI simulation model.*

Parameters	Values
Number of Electrodes	8
Electrodes' width	10.95 cm
Operating Frequency	2.4 GHz
Power	0 dbm / 1 mw
Diameter size (air)	200cm x 200cm
Dielectric properties of air	Conductivity: 0 Relative Permittivity: 1
Dielectric properties of human	Conductivity: 1.77 Relative Permittivity: 52.97

4. MODELLING AND SIMULATION CRITERA: ELECTRODES

In this section, t The electrode's width, w, is modelled and calibrated using (??) [5]. To get the cutoff frequency, substitute the appropriate electrode width and relative permittivity into (??) using ε_r (unitless). RF can propagate through the medium if the cutoff frequency is lower than the frequency of the RF signals employed in this work. This study's electrode's width, w is 10.95 cm. With $c_0 = 3 \times 10^8 ms^{-1}$ is the speed of light in vacuum.

$$f_c = \frac{c_0}{2w\sqrt{\varepsilon_r}} \tag{2}$$

Next, In this simulation research, the electrode runs at 2.4 [6]. Human formation is under this work's consideration. So, 2.4 GHz low frequency is useful for resolving larger objects [7]. Additionally, 2.4 GHz was chosen as the minimum measuring frequency because to the high relative permittivity of people, which is brought on by their high blood content and causes increased attenuation as frequency increases. In addition, the system operates at low electromagnetic frequencies enhance electromagnetic penetration with the certain amount of power applied. They are less susceptible in lossy material [8]. Finally, the study's transmission power is limited to either 0 dBm or 1 mW. This limitation was implemented in order to protect the researcher from radiation and heat[8]. Low power RF systems are typically significantly safer to operate. In addition, the prescribed transmission power can avoid human heating, which alters the morphology and dielectric characteristics of the organism during use. The results could be impacted by a minor change in the human shape and dielectric characteristics. The simulation model for RTI system is detailed out below in term of human with different setup configuration, simulation parameters for air, human and the fundamental equation. The parameters used in this simulation are summarized in Table 1. Besides, the measuring strategies and S-parameters are described in solving the forward problem.

***Table 2**: 2.4 GHz electrical characteristics of human tissues.*

Tissues	Relative Permittivity (ϵ)	Conductivity (S/m)
Human Skin (dry)	38	1.46
Human Fat tissue	5.3	0.11
Human Muscle tissue	52.7	1.77
Human Cortical Bone tissue	11.35	0.40

5. MODELLING AND SIMULATION CRITERA: HUMAN

It is well recognised that iron is a necessary component of the human body. The distribution of iron inside the body is as follows: 1800 mg circulating red blood cells; 300 mg bone marrow; 300 mg muscle; 600 mg splenic macrophages; and 1000 mg liver; with 20-25 mg iron cycles daily [22]. Nowadays, electromagnetic (EM) interference pollution, which may be detrimental to humans, has received a lot of attention [23], [24]. The red blood cell is an integral element of the human body and plays a crucial function in maintaining a healthy human body [25]. This study looked at the RF absorption characteristics of healthy human blood. The complex permittivity, permeability, and reflection loss of human blood are evaluated in frequency using a vector network analyzer (VNA).

The reflection loss (RL) is calculated using the values of permeability and permittivity (real and imaginary portions) (??). Transmission line theory and the Nicholson-Ross-Weir (NRW) formula were used to compute and simulate reflection loss (RL) using data from electromagnetic characteristics (4) [26].

$$RL\,(dB) = 20log\left|\frac{Z_z - 1}{Z_z + 1}\right| \tag{3}$$

$$Z_z = \sqrt{\frac{\mu_r}{\varepsilon_r}}tanh\left(j\frac{2\pi f d}{c}\sqrt{\mu_r \varepsilon_r}\right) \tag{4}$$

$$\mu = \mu' - j\mu'' \;\; (permeability)$$

$$\varepsilon = \varepsilon' - \varepsilon'' \;\; (permittivity)$$

where Z_z is the normalised input impedance in relation to the free space impedance d is the blood The velocity of light and the frequency of RTI in free space are represented by thickness c and f, respectively. Table 2 [9] displays at 2.4 GHz, the relative permittivity (ε) and conductivity (σ) of many human tissues, including skin, fat, and muscle [10]. As seen in Table 2, fat tissue has much lower permittivity and conductivity than other tissues.

6. MODELLING THE ELECTROMAGNETIC BEHAVIOUR

Maxwell's equations regulate electric (E) and magnetic (H) field propagation in macroscopic, isotropic, linear, and non-dispersive material. Equations (5) to (11) [11]. Their time-harmonic form are given by:

$$Faraday's Law: \ \nabla\times \mathrm{E}(\mathrm{r}) = -\mathrm{j}\omega \mathrm{B}(\mathrm{r}) \tag{5}$$

$$Ampere's Law: \nabla\times \mathrm{H}(\mathrm{r}) = \mathrm{j}\omega \mathrm{D}(\mathrm{r}) + \mathrm{J}(\mathrm{r}) \tag{6}$$

$$Gauss Law: \nabla.\mathrm{B}(\mathrm{r}) = 0 \tag{7}$$

$$Gauss Law: \nabla.\mathrm{D}(\mathrm{r}) = \rho \tag{8}$$

where E is the electric field intensity $\left(\frac{V}{m}\right)$,H is the magnetic field intensity $\left(\frac{A}{m}\right)$, B is the magnetic flux density *(T), D* is the electric flux density $\left(\frac{C}{m^2}\right)$, J is the electric current density $\left(\frac{A}{m^2}\right)$, ρ is the electric charge density $\left(\frac{C}{m^3}\right)$ and r indicates the position vector

There equations depend implicitly on e^{jwt}, where $j = \sqrt{-1}$ denotes the imaginary units. In the presence of material in which electromagnetic events occur, constitutive relations have been utilised.

$$D(r) = \varepsilon_0 \varepsilon_\mathrm{r} \mathrm{E}(\mathrm{r}) \tag{9}$$

$$J(r) = \sigma \mathrm{E}(\mathrm{r}) \tag{10}$$

$$B(r) = \mu_0 \mu_\mathrm{r} \mathrm{H}(\mathrm{r}) \tag{11}$$

where μ_0 is the permeability of free space $\left(\frac{H}{m}\right)$, μ_r is the relative permeability. Below is the derivation of the equation used by the software solver. (11) is substituted into (8) and curl both sides as shown in (12).

$$\nabla\times(\nabla\times \mathrm{E}(\mathrm{r})) = -\mathrm{j}\omega\mu_0\mu_\mathrm{r}(\nabla\times \mathrm{H}(\mathrm{r})) \tag{12}$$

Substitute (6), (9), and (10) into (12)

$$\nabla\times(\nabla\times \mathrm{E}(\mathrm{r})) = -\mathrm{j}\omega\mu_0\mu_\mathrm{r}\left(\mathrm{j}\omega\varepsilon_0\varepsilon_\mathrm{r}\mathrm{E}(\mathrm{r}) + \sigma \mathrm{E}(\mathrm{r})\right) \tag{13}$$

$$\nabla\times(\nabla\times \mathrm{E}(\mathrm{r})) = \omega^2\mu_0\mu_\mathrm{r}\varepsilon_0\varepsilon_\mathrm{r}\mathrm{E}(\mathrm{r}) - \mathrm{j}\omega\mu_0\mu_\mathrm{r}\sigma\mathrm{E}(\mathrm{r}) \tag{14}$$

This equation is simplified to Equation (15) and Equation (16)

$$\nabla\times(\nabla\times \mathrm{E}(\mathrm{r})) = \mathrm{k}_0^2\mu_\mathrm{r}\left(\varepsilon_\mathrm{r} - \mathrm{j}\frac{\sigma}{\varepsilon_0\omega}\right)\mathrm{E}(\mathrm{r}) \tag{15}$$

$$\nabla\times\mu_\mathrm{r}^{-1}(\nabla\times \mathrm{E}(\mathrm{r})) - \mathrm{k}_0^2\left(\varepsilon_\mathrm{r} - \mathrm{j}\frac{\sigma}{\varepsilon_0\omega}\right)\mathrm{E}(\mathrm{r}) = 0 \tag{16}$$

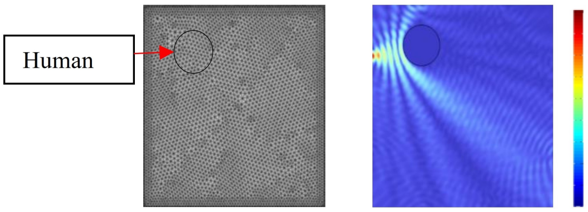

(a) *(b)*

Fig. 4*: (a) RTI's mesh pattern, (b) When a 2.4 GHz RF sensor node is emitting, normalise the electric field.*

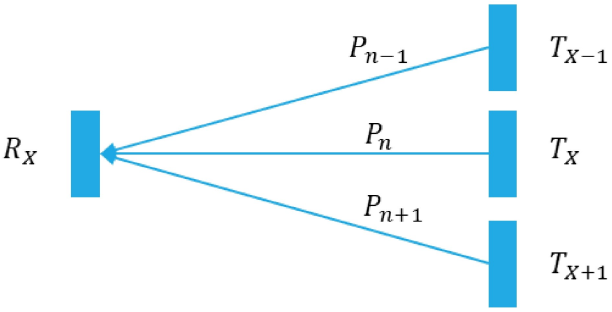

Fig. 5*: Normal tomography projection.*

where $k_0 = \omega\sqrt{(\mu_0\varepsilon_0)}$ is free space wave. In this work, in order to apply a scalar model to the RTI problem, various assumptions must be made.

7. FORWARD MODEL'S SOLUTION

The theoretical scattered electromagnetic subject measurements computed at each antenna are evaluated using the forward issue. The discretized electric powered area strength is addressed using an instantaneous form of solver that is primarily dependent on the distribution of human insulating qualities, air, and electromagnetic stimulation in terms of frequency. As illustrated in Fig. 4, the electrical issue is converted into one that is calculated on a mesh (a).

The sector values and the dielectric are described by the mesh system[12]. Fig. 4 depicts the calculation of the completely electric-powered field using a forward solver from a person (b). While there are no people in the rice for each of the interest antennas, the incidence electric field is the electrical field.

8. ADJACENT CRITERION METHOD

A strategy for enhancing spatial resolution in tomography is provided by [13]. The suggested approach changes back-projection technique in reconstruction tomography images. Fig. 5 depicts the projection array of a typical tomography system. In Fig. 5, three transmitters, T_x transmits RSS within angle θ to one receiver R_x along projection path P_n. Due to the reflection of RSS at the human subject, therefore it generates a shadow across the projection path behind the human.

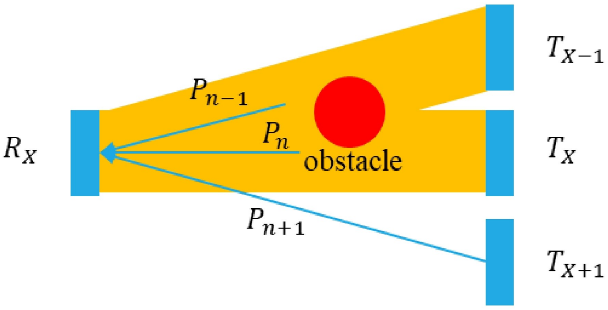

***Fig. 6**: Traditional back-projection.*

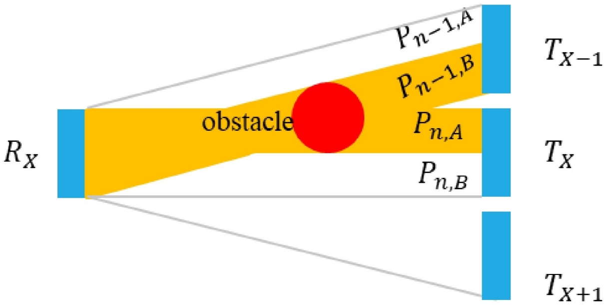

***Fig. 7**: Adjacent Criterion Method back-projection.*

In Fig. 6, the projection path is back-projected using the traditional back-projection approach by multiplying the attenuation RSS by its projection matrix. The concept behind this study is that the RSS penetrates the air medium and is totally reflected at the human interface.

Assuming the original phantom's information is binary, the signal on the receivers displays how much RSS has been "shadowed" by the obstacles. A high and low RSS (RSS_{TL} and RSS_{TH}) is introduced in order to increase the number of effective receivers (P_A and P_B). In the proposed method, Each projection was separated into two path A, ($P_{n,A}$) and path B, ($P_{n,B}$) as shown in Fig. 7. When receiving happens, the transmission sensors will operate in accordance with the ACM truth rules shown in Table 3.

The number of projections is nearly doubled when using the ACM technique. When there is no human in the projection path, normalised receiving RSS is 0. For a human greater than the sensor's angle, the normalised receiving RSS is 1. However, when the human is between two sensor, threshold values are used. The high (RSS_H) and low (RSS_L) RSS provide adequate detection of human presence along the relevant path transmission. The ACM approach used to increase the performance of LBP, FBP, Gaussian, NOSER, and Tikhonov algorithms. As a result, the projection artefacts that are frequent in back-projection.

***Table 3**: Adjacent Criterion Method (ACM) Truth Table.*

Sensor Loss (RSS)	Condition	Active Projection	
		$P_{n,A}$	$P_{n,B}$
$0 \leq RSS_{TX} \leq RSS_{TL}$	x	0	0
$RSS_{TL} \leq RSS_{TX} \leq RSS_{TH}$	$P_{n-1,B}$=0	0	1
	$P_{n-1,B}$=1	1	0
$RSS_{TL} \leq RSS_{TX} \leq 1$	x	1	1

9. RESULTS AND DISCUSSION

Provide simulated findings following the experimental results. This is because the experimental data was utilised to define the simulation settings in order to make them as realistic as feasible.

9.1 Performance Metrics

There are several techniques exist for evaluating the quality of the reconstructed images. Generally, the reconstructed image is evaluated by comparing it to the reference image. In this work, an unbiased and automated objective assessment were performed with intention of determining MSSIM between the reference image and reconstructed images. It provides a reliable result to all assigned parameters.

Mean square error (MSE), peak signal-to-noise ratio (PSNR), and mean structural similarity index (MSSIM) are three regularly used image quality evaluation techniques. [14] stated that MSE is a technique which has been used widely to assess the quality and fidelity of images. The solution for MSE is expressed in (17).

$$MSE\,(x,y) = \frac{1}{N}\sum_{i=1}^{N_i}(e_i)^2 \tag{17}$$

$$e_i = \mathrm{x_i} - \mathrm{y_i} \tag{18}$$

where N is the number of pixels of the image and $e_i$is the difference between two images one the reference image and reconstruction image. When MSE approaches zero, it means that the reconstructed image is identical to the original images. MSE often being converted into peak signal-to-noise ratio (PSNR) in image processing [14]. When MSE approaches zero, PSNR value is approaching infinity. The higher the value of PSNR, the higher the quality of the image [15]. The solution for PSNR is expressed in (19).

$$PSNR = 10\log_{10}\frac{L^2}{MSE} \tag{19}$$

where L is the dynamic range of acceptable image pixel intensities The usefulness of PSNR is depending on the comparison of images with different value of L, otherwise it contains no new information relative to the MSE [14].

The mean structural similarity index (MSSIM) is a tool for comparing the similarity of two images, the reference image and the reconstructed image. Structure, intensity,

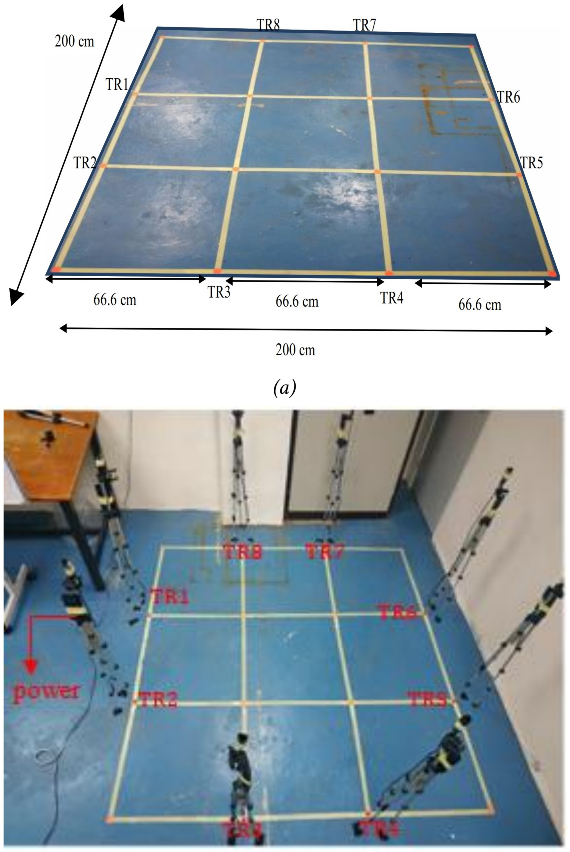

(a)

(b)

***Fig. 8**: (a) Surface Zone of the experiment, (b) The actual experiment condition.*

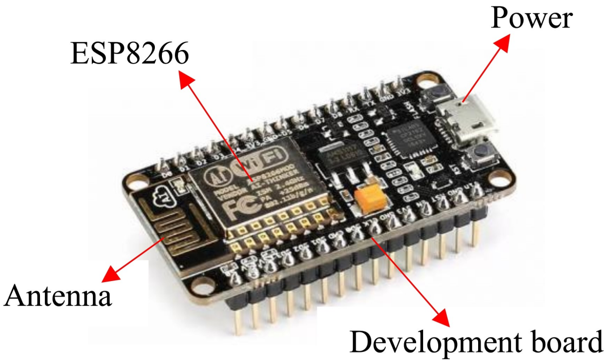

***Fig. 9**: RF sensor node in the RTI system.*

and contrast are used to assess images. It produces an index ranging from 0 to 1. When the reconstructed picture is identical to the real image, its output index equals one. The solutions for MSSIM are expressed in (20) and (21).

$$MSSIM(X,Y) = \frac{1}{M}\sum_{J=1}^{M} SSIM(x_r, y_r) \qquad (20)$$

$$SSIM(x,y) = [\mathrm{l(x,y)}]^{\alpha}[\mathrm{c(x,y)}]^{\beta}[\mathrm{s(x,y)}]^{\gamma} \qquad (21)$$

where X is the reference image, Y is the reconstructed image, x and y are the image contents at the local window and M is the number of local windows of the image $l(x,y)$, $c(x,y)$ and $c(x,y)$ are the luminance, contrast and structure comparison function with α, β and γ as parameters to adjust their relative importance respectively. This technique is an objective method which can quantify subjective image quality more effectively compared MSE and PSNR [14], [15]. It is due to MSE and PSNR show a poor correlation between their result and the human eye's judgment [15].

9.2 Comparison and Analysis of Reconstruction Results with Different Algorithms

If the RF node does not settle on an accurate place, the accuracy of the results may suffer. Furthermore, it will cause position adjustments and may transmute and impact the reading. As a result, the simplest solution to address such issues was to utilise a tripod platform to standardise the height and stable all RF nodes from the floor, as illustrated in Fig. 8. (b). The stands are 120cm above the floor, and the RF node is attached to them. The rationale for placing the RF node 120 cm above the floor is to minimise fluctuations in the RSS value [16]–[19]. The ground reflection model describes how the odds of the RSS value fluctuating are increased when the RF node is situated on the floor.

The hardware of the system is designed based on RF sensor nodes with a frequency of 2.4 GHz, using sensor WiFi model namely NodeMCU (Node MicroController Unit) is an open-source software and hardware development environment based on the ESP8266, a low-cost System-on-a-Chip (SoC), as seen in Fig 9. The Espressif Systems ESP8266 comprises all of the essential components of a computer: CPU, RAM, networking (WiFi), and even a contemporary operating system and SDK. The parameters of the ESP8266 RF module are shown in Table 4.

The reconstruction results from various methods for three distinct human locations were analysed to assess the efficacy of the suggested ACM-based image reconstruction technique in overcoming the inverse problem caused by the decreased sensor model to 8 sensors in a big tomography system. Fig. 11 depicts the picture reconstruction results acquired from simulation data, whereas Figure The picture reconstruction findings acquired from experimental data are shown in Fig.12.

To test the performance of the reconstruction methods, certain simulation experiments were conducted. To replicate the various human localization distributions, three phantoms were employed as models. The phantoms were chosen as a broad depiction of humans in the monitoring region, and they are distributed as single people (simulation model 1), two people (simulation model 2), and three people (simulation model 3). The

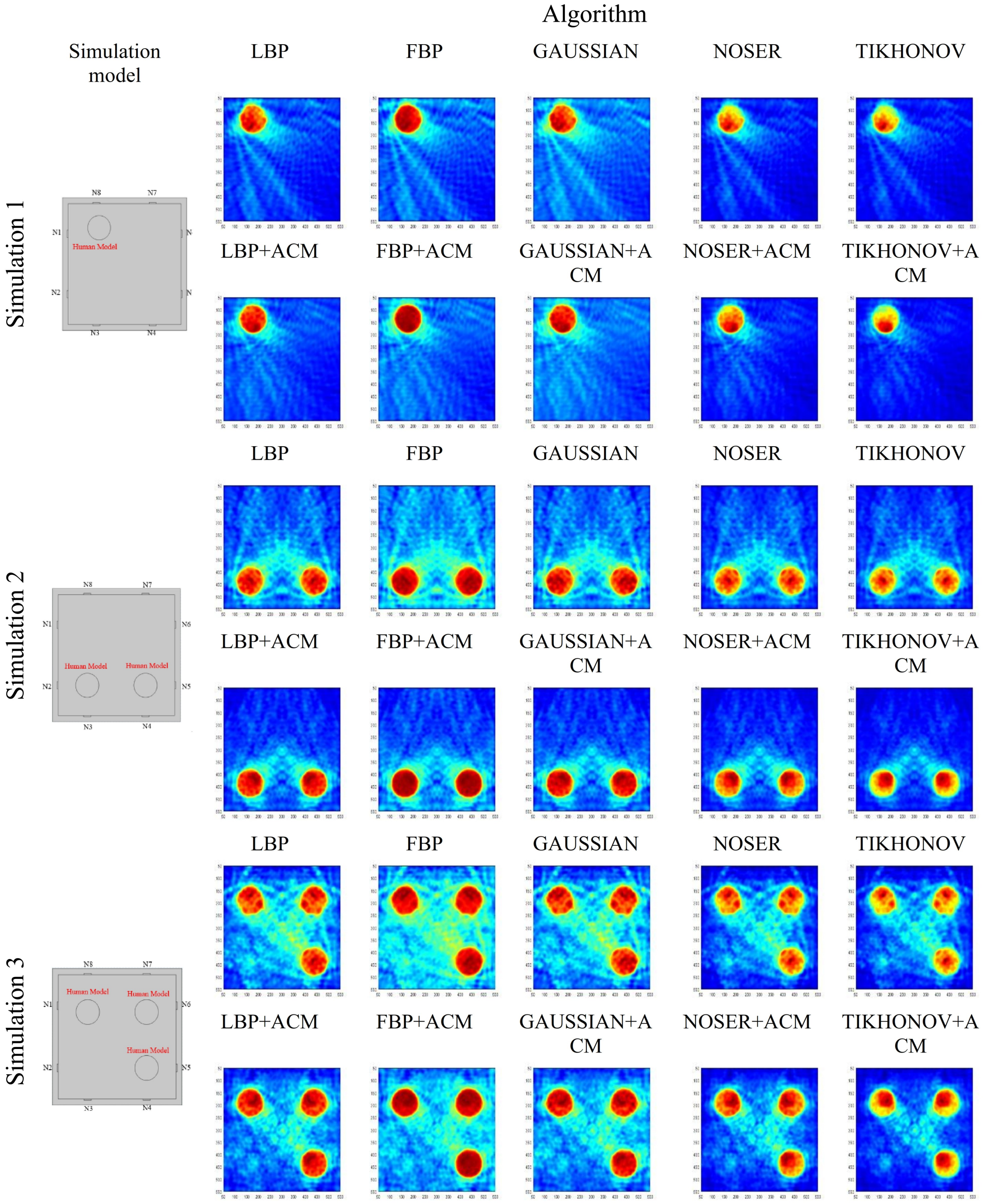

Fig. 10: Image reconstruction simulation results in 2D view.

reconstruction outcomes of several methods for three distinct human locations have been investigated. The image reconstruction results acquired from simulation data are shown in Fig. 10, and the image reconstruction results obtained from experimental data are shown in Fig. 11.

The LBP, FBP, GAUSSIAN, NOSER, TIKHONOV, LBP + ACM, FBP + ACM, GAUSSIAN+ ACM, NOSER+ ACM, and TIKHONOV+ ACM algorithms were all tried on phantoms and the results were analysed. Figs. 10 and 11 depict the image reconstruction modelling and experimental findings in 2D. The ACM approach, on the

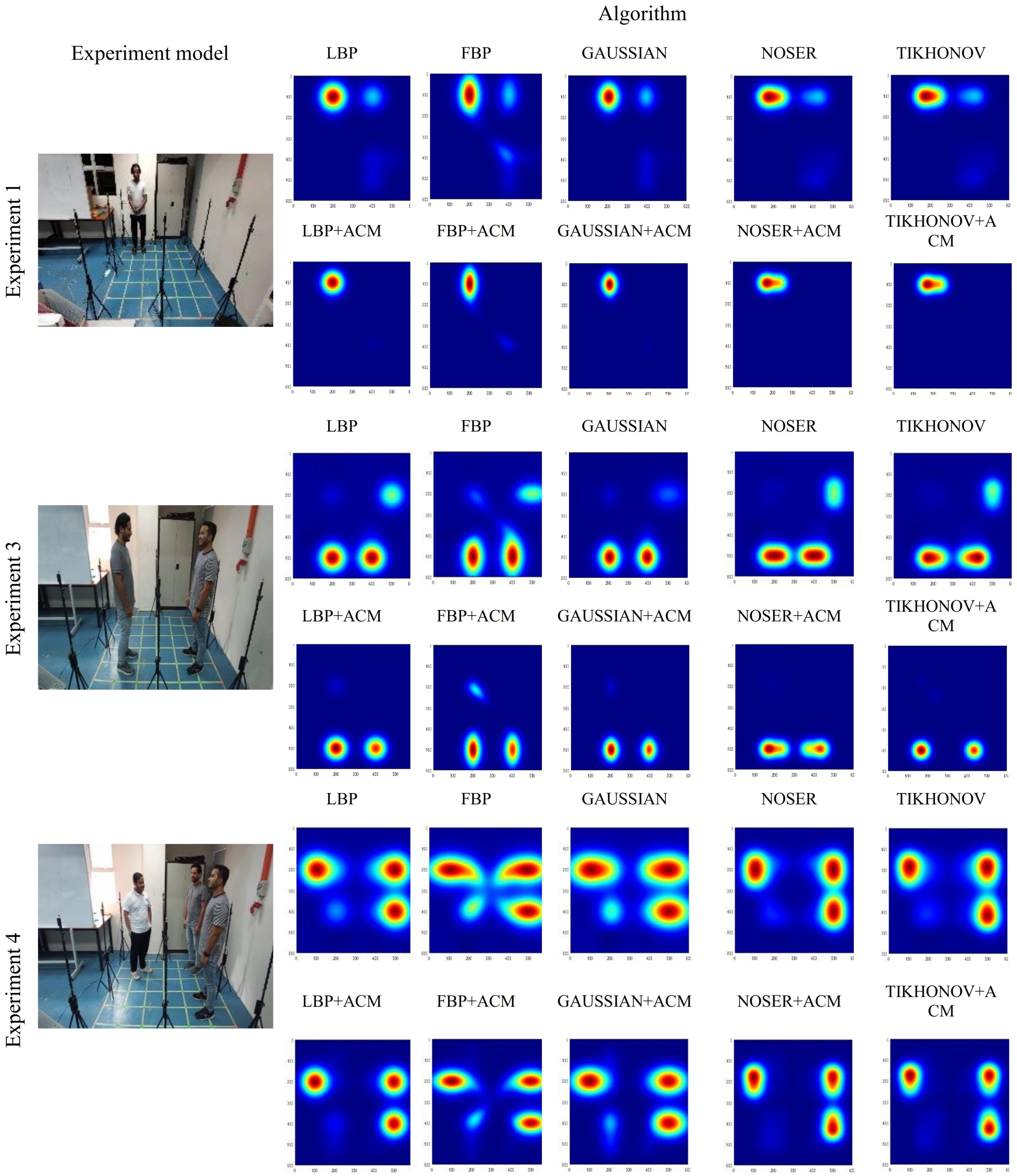

Fig. 11*: Image reconstruction experimental results in 2D view.*

other hand, improves tomogram image. According to Fig. 10, Fig. 10 ACM methods improved performance by up to 34% . The ACM approach doubles the projection data, increasing spatial resolution. However, there is a disadvantage to ACM. As the projection data accumulates, the image becomes more susceptible to noise from more projection artefacts. This is visible in concentration differential measurements. Among the reconstruction techniques, the ACM method improved the percentage difference estimated on all simulated and experimental results. MSSIM, PSNR, and MSE, on the other hand, are primarily concerned with perceptual image measurement and are hence unaffected by the reconstructed simulation results through each image reconstruction algorithm subjectively demonstrate decent overall image quality indexes for all simulated models. The maximum

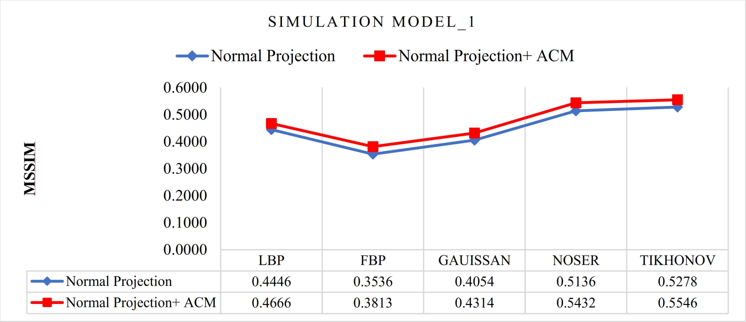

Fig. 12: MSSIM Indexes measured on simulation model 1.

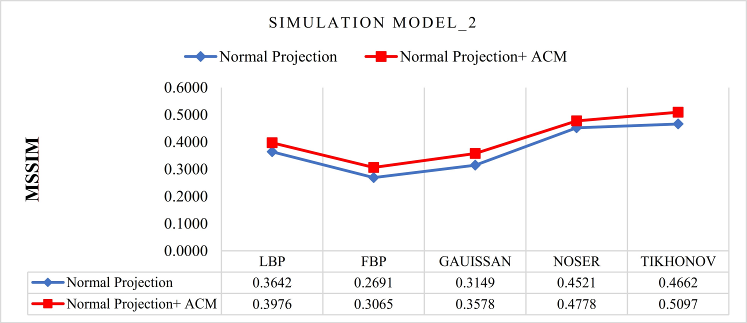

Fig. 13: MSSIM Indexes measured on simulation model 2.

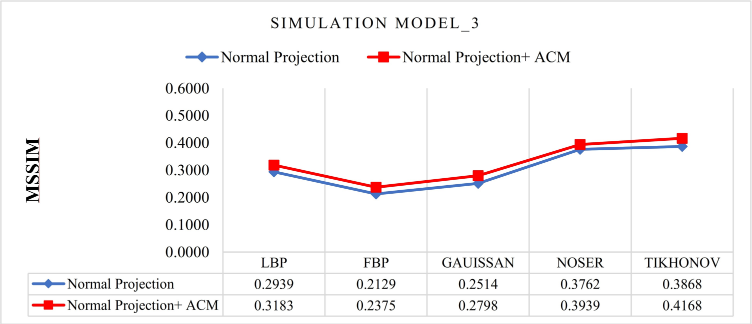

Fig. 14: MSSIM Indexes measured on simulation model 3.

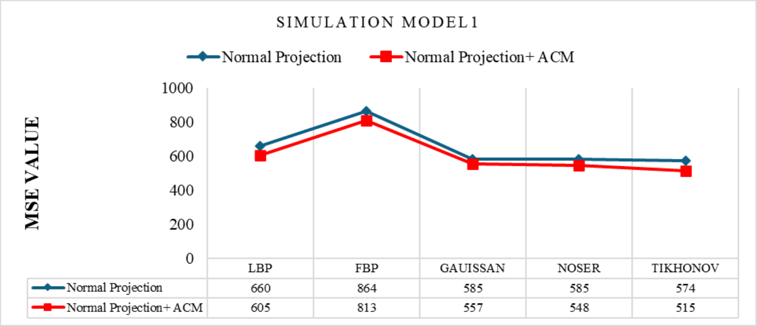

Fig. 15: MSE Indexes measured on simulation model 1.

score of the MSSIM index is 0.5546 of simulated model 1 using the TIKHONOV+ACM algorithm, whereas the minimum score of the MSSIM index is 0.2129 of simulated model 3 using the FBP algorithm. For the MSE index, the maximum score is 515 of simulated model 3 using the TIKHONOV+ACM algorithm, while the minimum score

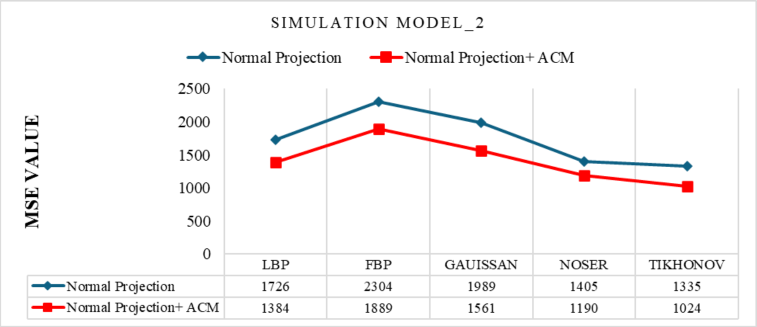

***Fig. 16**: MSE Indexes measured on simulation model 2.*

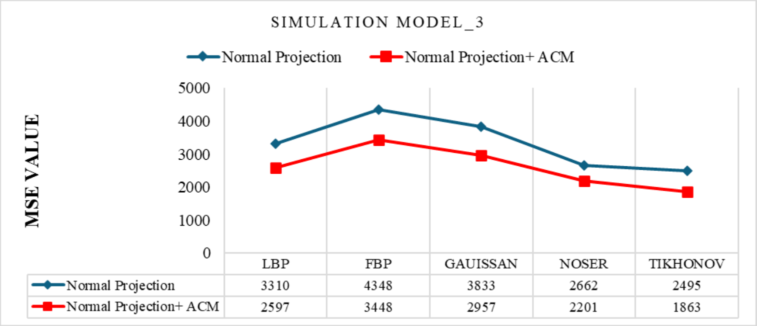

***Fig. 17**: MSE Indexes measured on simulation model 3.*

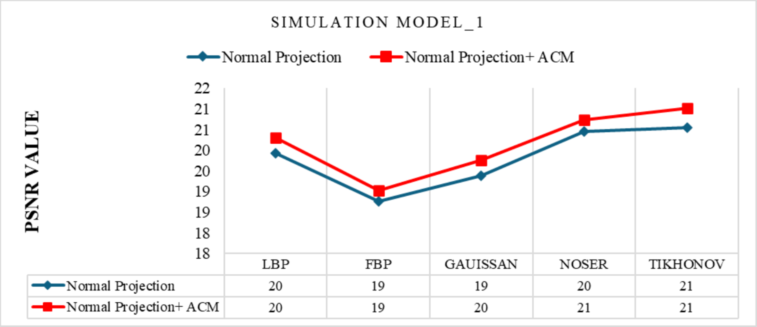

***Fig. 18**: PSNR Indexes measured on simulation model 1.*

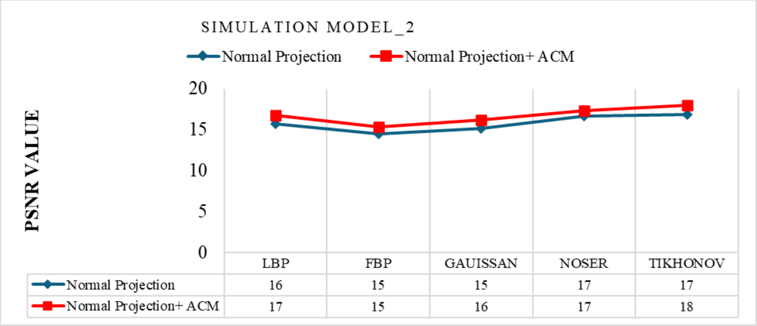

***Fig. 19**: PSNR Indexes measured on simulation model 2.*

of the MSE index is 4348 of simulated model 1 using the FBP algorithm.

Lastly, PSNR index, the maximum score is 20.8 of simulated model 1 using the LBP+ ACM algorithm, while the minimum score of the PSNR index is 12 of simulated model 3 using the FBP algorithm. Regarding the

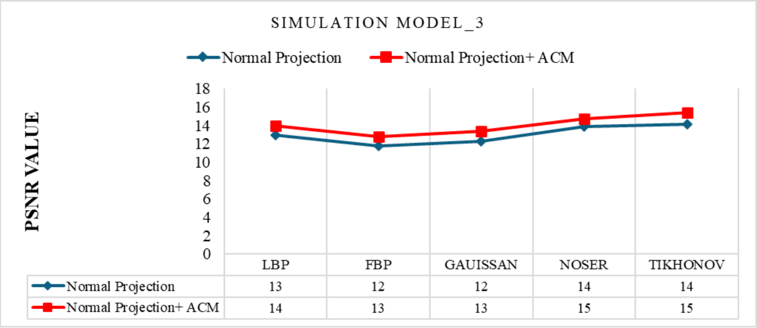

Fig. 20: *PSNR Indexes measured on simulation model 3.*

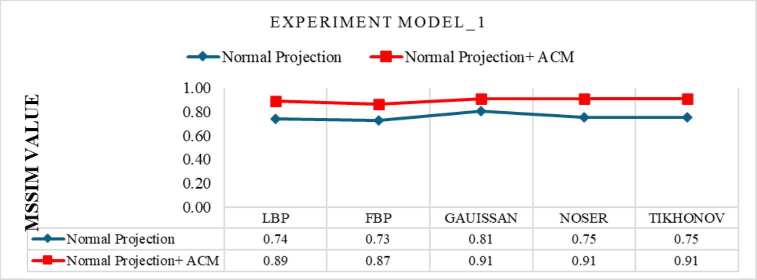

Fig. 21: *MSSIM Indexes measured on Experimental model 1.*

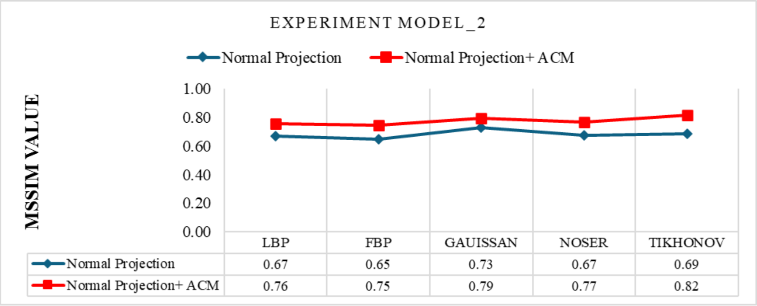

Fig. 22: *MSSIM Indexes measured on Experimental model 2.*

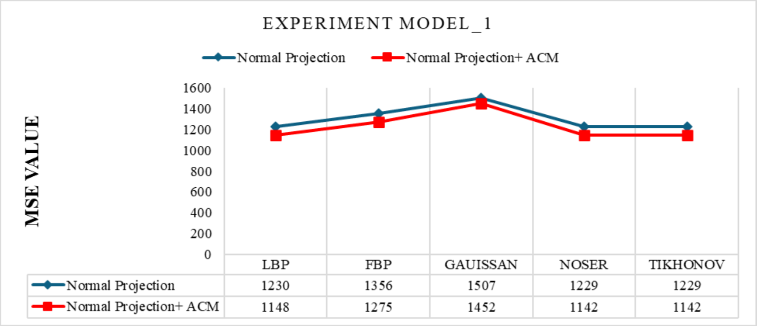

Fig. 23: *MSSIM Indexes measured on Experimental model 3.*

image reconstruction algorithms, the TIKHONOV+ACM algorithm constantly recorded the highest MSSIM value among the phantom studies, surpassing all the other algorithms. In contrast, the lowest MSSIM value is always measured by the FBP algorithm, the image reconstruction algorithms, the TIKHONOV+ACM algorithm constantly recorded the highest MSE value among the phantom studies, surpassing all the other algorithms. In contrast, the lowest MSE value is always measured by the FBP algorithm, finally the image reconstruction algorithms,

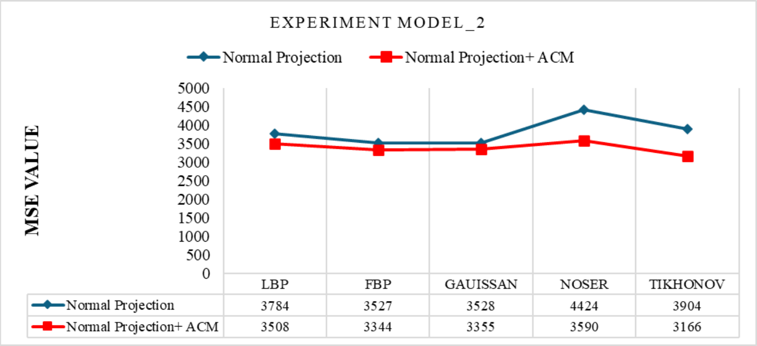

Fig. 24: MSE Indexes measured on Experimental model 1.

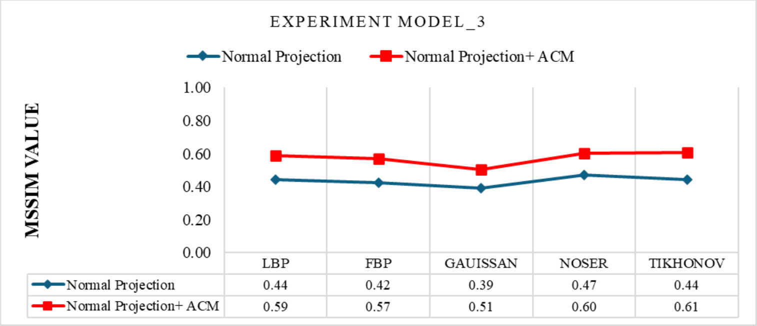

Fig. 25: MSE Indexes measured on Experimental model 2.

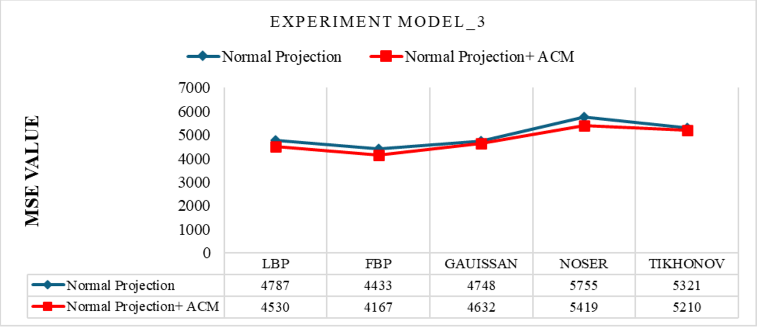

Fig. 26: MSE Indexes measured on Experimental model 3.

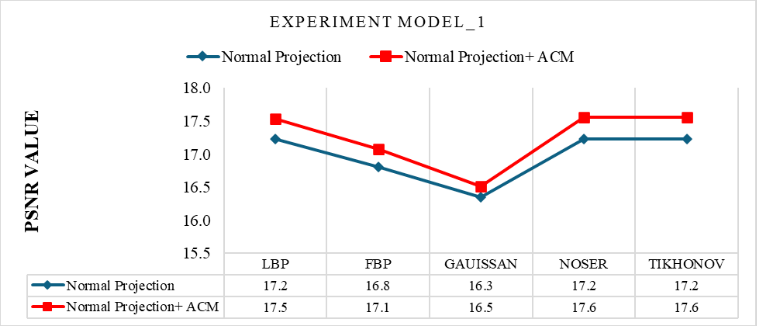

Fig. 27: PSNR Indexes measured on Experimental model 1.

the LBP+ ACM algorithm constantly recorded the highest PSNR value among the phantom studies, surpassing all the other algorithms. In contrast, the lowest PSNR value is always measured by the FBP algorithm.

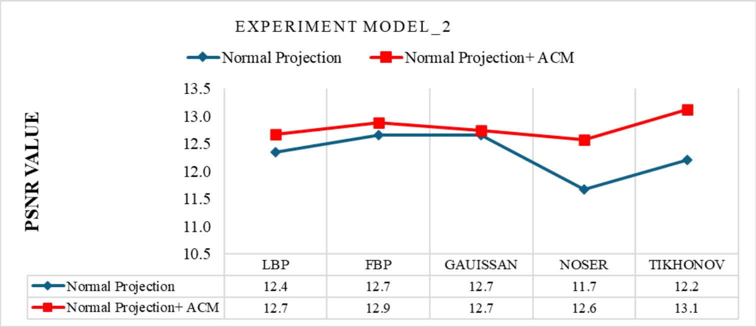

Fig. 28: *PSNR Indexes measured on Experimental model 2.*

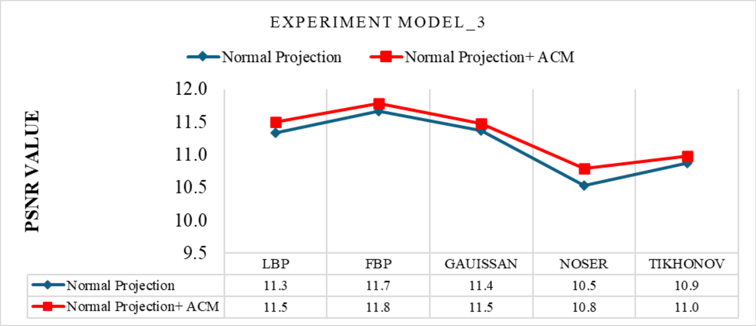

Fig. 29: *PSNR Indexes measured on Experimental model 3.*

Table 4: *Specifications of RF sensor node.*

Items	Parameters
Certification	Wi-Fi Alliance
Protocols	802.11 b/g/n (HT20)
Frequency Range	2.4 GHz ~ 2.5 GHz (2400 MHz ~ 2483.5 MHz)
TX Power	802.11 b: +20 dBm
	802.11 g: +17 dBm
	802.11 n: +14 dBm
Rx Sensitivity	802.11 b: –91 dbm (11 Mbps)
	802.11 g: –75 dbm (54 Mbps)
	802.11 n: –72 dbm (MCS7)
Antenna	PCB Trace, External, IPEX Connector, Ceramic Chip
Operating Voltage	2.5 V ~ 3.6 V

The reconstructed experimental results through each image reconstruction algorithm subjectively demonstrate decent overall image quality indexes for all experimental models. The maximum score of the MSSIM index is 0.5546 of experimental model 1 using the TIKHONOV+ACM algorithm, whereas the minimum score of the MSSIM index is 0.2129 of experimental model 3 using the FBP algorithm. For the MSE index, the maximum score is 1142 of experimental model 1 using the TIKHONOV+ACM algorithm, while the minimum score of the MSE index is 5755 of experimental model 3 using the NOSER algorithm. Lastly, PSNR index, the maximum score is 17.6 of experimental model 1 using the NOSER+ ACM and TIKHONOV + ACM algorithm, while the minimum score of the PSNR index is 10.5 of experimental model 3 using the NOSER algorithm. Regarding the image reconstruction algorithms, the TIKHONOV+ACM algorithm constantly recorded the highest MSSIM value among the phantom studies, surpassing all the other algorithms. In contrast, the lowest MSSIM value is always measured by the FBP algorithm, the image reconstruction algorithms, the TIKHONOV+ACM algorithm constantly recorded the highest MSE value among the phantom studies, surpassing all the other algorithms. In contrast, the lowest MSE value is always measured by the NOSER algorithm, finally the image reconstruction algorithms, the NOSER+ ACM and TIKHONOV + ACM algorithm constantly recorded the highest PSNR value among the phantom studies, surpassing all the other algorithms. In contrast, the lowest PSNR value is always measured by the NOSER algorithm.

ACM techniques improved performance by up to 34%. The ACM approach doubles the projection data, increasing spatial resolution. However, there is a disadvantage to ACM. As the projection data accumulates, the image becomes more susceptible to noise from more projection artefacts. This is visible in concentration differential measurements. The ACM percentage difference obtained on all simulated pictures by ACM approach was increased

***Table 5**: MSSIM, MSE and PSNR simulated percentage (%) improvement by ACM algorithms.*

Technique	No	LBP+ ACM	FBP+ ACM	GAUSSIAN+ ACM	NOSER+ ACM	TIKHONOV +ACM
MSSIM	1	4.9	7.8	6.4	5.8	5.1
	2	9.2	13.9	13.6	5.7	9.3
	3	8.3	11.6	11.3	4.7	7.7
MSE	1	8.3	5.8	4.7	6.2	10.3
	2	19.8	18.0	21.5	15.3	23.3
	3	21.5	20.7	22.8	17.3	25.3
PSNR	1	1.9	1.4	1.9	1.4	2.3
	2	6.1	5.9	7.0	4.3	6.8
	3	8.1	8.6	9.2	5.9	9.0

***Table 6**: MSSIM, MSE and PSNR experimental percentage (%) improvement by ACM algorithms.*

Technique	No	LBP+ ACM	FBP+ ACM	GAUSSIAN +ACM	NOSER+ ACM	TIKHONOV +ACM
MSSIM	1	20.4	19.1	12.8	20.5	20.5
	2	13.4	15.3	8.6	14.1	19.3
	3	33.0	34.4	29.3	27.3	36.5
MSE	1	6.7	6.0	3.7	7.1	7.1
	2	7.3	5.2	4.9	18.9	18.9
	3	5.4	6.0	2.4	5.8	2.1
PSNR	1	1.7	1.6	1.0	1.9	1.9
	2	2.7	1.8	0.7	7.8	7.4
	3	1.5	1.1	0.9	2.5	1.0

among the reconstruction algorithms. MSSIM, on the other hand, is primarily concerned with perceptual image measurement and is hence unaffected by noise. The improvement achieved by ACM algorithms are shown in Table 5 where the minimum percentage improvement for MSSIM is 4.9 % at simulation model 1, the minimum percentage improvement for MSE is 4.7 % at simulation model 1 and the minimum percentage improvement for PSNER is 1.4 % at simulation model 1. The highest of MSSIM is 13.9 % at simulation model 1, The highest of MSE is 25.3 % at simulation model 2 and the highest of PSNER is 9.2 % at simulation model 3.

Table 6 shows that the ACM approach greatly improves the MSSIM index. As a result, utilising the ACM approach adds an advantage to the current reconstruction technique. Table 6 summarised the ACM technique's improvement as assessed by the MSSIM, MSE, and PSNER indexes. The improvement of MSSIM had increased up to 36.5 %, 34.4 %, 33.0 %, 29.3 % and 27.3 % using TIKHONOV+ACM, FBP + ACM, LBP + ACM, GAUSSIAN+ACM and NOSER+ACM respectively. The improvement of MSE had increased up to 18.9%, 18.9%, 7.3%, 6.0% and 4.9% using TIKHONOV+ACM, NOSER+ACM, LBP + ACM, FBP + ACM, and GAUSSIAN+ACM respectively. The improvement of PSNER had increased up to 7.8%, 7.4%, 2.6%, 1.8% and 1% using NOSER+ACM, TIKHONOV+ACM, LBP + ACM, FBP + ACM, and GAUSSIAN+ACM respectively.

10. CONCLUSIONS

A radio tomography system for human localisation was successfully constructed, and its performance was evaluated and analysed. The Adjacent Criterion Method (ACM) technique was created to address the problem of low spatial resolution images by virtually expanding the projection data. The spatial resolution was enhanced and the reconstructed tomograms were more precise after splitting the projection path in two. Several experiments were conducted and the results had showed encouraging improvement in tomogram reconstruction using ACM method.

ACKNOWLEDGEMENT

The authors would like to acknowledge the support from the Transdisciplinary Research Grant Scheme (TRGS) under grant number of TRGS/1/2018/UNIMAP/02 /4/2 from the Ministry of Higher Education Malaysia. The authors would also gratefully thank Universiti Malaysia Perlis, Malaysia for the facilities and technical assistance.

REFERENCES

[1] G. T. Nafziger, "Wireless Sensor Network Optimization for Radio Tomographic Imaging," Mar. 2020.

[2] N. A. M. Ramli et al., "A Design and Development of a Wireless Sensor Network for Potential Monitoring and Localization," *J. Electr. Eng. Technol.*, August 2020.

[3] C. Zhu, J. Wang, and Y. Chen, "ARTI (Adaptive radio tomographic imaging): One new adaptive elliptical weighting model combining with tracking estimates," *Sensors (Switzerland)*, vol. 19, no. 5, 2019.

[4] M. S. M. Abdullah, M. H. Fazalul Rahiman, L. M. Kamarudin, L. Mohamed, and A. Zakaria, "Simulation of Radio Tomographic Imaging for Measurement Rice Moisture Content," in *2020 10th IEEE International Conference on Control System, Computing and Engineering (ICCSCE)*, 2020, pp. 62–67. August 2020.

[5] M. Mallach, P. Gebhardt, and T. Musch, "2D microwave tomography system for imaging of multiphase flows in metal pipes," *Flow Meas. Instrum.*, vol. 53, pp. 80–88, March 2017.

[6] H. H. Hinrikus and J. R. Riipulk, "Microwave Imaging.," *Conf. Proc. - Eur. Microw. Conf.*, pp. 706–711, 2006.

[7] A. Fhager, P. Hashemzadeh, and M. Persson, “Reconstruction quality and spectral content of an electromagnetic time-domain inversion algorithm,” IEEE *Trans. Biomed. Eng.*, vol. 53, no. 8, pp. 1594–1604, 2006.

[8] A. T. Mobashsher and A. M. Abbosh, “Developments of tomography and radar-based head imaging systems,” *2015 Int. Symp. Antennas Propagation, ISAP 2015*, no. C, pp. 292–294, April 2016.

[9] M. Vallejo, J. Recas, P. G. del Valle, and J. L. Ayala, “Accurate human tissue characterization for energy-efficient wireless on-body communications,” *Sensors (Switzerland)*, vol. 13, no. 6, pp. 7546–7569, 2013.

[10] M. Di Renzo, R. M. Buehrer, and J. Torres, “Pulse Shape Distortion and Ranging Accuracy in UWB – based Body Area Networks for Full – Body Motion Capture and Gait Analysis,” 2007.

[11] A. Abdullah, N. K. Nik Ismail, T. A. Abdul Kadir, J. Md Zain, N. A. Jusoh, and N. Mohd Ali, “Agar Wood Grade Determination System Using Image Processing Technique,” *Proc. Int. Conf. Electr. Eng. Informatics*, pp. 427–429, January 2007.

[12] D. G. Drogoudis, G. A. Kyriacou, and J. N. Sahalos, “Microwave tomography employing an adjoint network based sensitivity matrix,” *Prog. Electromagn. Res.*, vol. 94, no. July 2014, pp. 213–242, 2009.

[13] M. H. F. Rahiman, R. A. Rahim, H. A. Rahim, and N. M. N. Ayob, “Novel adjacent criterion method for improving ultrasonic imaging spatial resolution,” *IEEE Sens. J.*, vol. 12, no. 6, pp. 1746–1747, June 2012.

[14] Z. Wang and A. C. Bovik, “Mean Squared Error : Love It or Leave It ?,” *IEEE Signal Process. Mag.*, vol. 26, no. 1, pp. 98–117, 2009.

[15] A. Horé and D. Ziou, “Image quality metrics: PSNR vs. SSIM,” *Proc. - Int. Conf. Pattern Recognit.*, no. March 2015, pp. 2366–2369, August 2010.

[16] M. S. M. Abdullah, M. H. F. Rahiman, N. S. Khalid, and A. S. A. Nasir, “Enhancing Indoor Radio Tomographic Imaging Based on Normal Distribution of Sigma to Reduce RF Nodes,” vol. 12, no. 1, pp. 125–141, 2024.

[17] M. S. M. Abdullah, M. H. F. Rahiman, N. S. Khalid, and A. S. A. Nasir, “Initial Study of Radio Tomographic Imaging for Human localization by using Simulation Model Initial Study of Radio Tomographic Imaging for Human localization by using Simulation Model,” *J. Phys. Conf. Ser.*, 2023.

[18] M. S. M. Abdullah et al., “Design and Development of RTI System for Moisture Content Localization in Rice Silo,” pp. 0–10, doi: https://doi.org/10.21203/rs.3.rs-1390879/v1.

[19] M. S. M. Abdullah, M. H. F. Rahiman, N. S. Khalid, and A. S. A. Nasir, “Attenuation Field Estimation Using Radio Tomography in Different System Models,” vol. 6, no. 2, pp. 25–32, 2023.

M. S. M. Abdullah received a B. Eng. (Hons) degree in Mechatronics Engineering at Universiti Malaysia Perlis and M. Sc. Degree in Mechatronics Engineering at Universiti Malaysia Perlis in 2018 and 2021 respectively. He is currently pursuing his Ph. D in Mechatronics Engineering at Universiti Malaysia Perlis. His research interests include Radio Tomographic Imaging, Internet of Things (IoT), Programming and sensor network. telecommunication.

M. H. F. Rahiman received the B.Eng. degree in electrical (control and instrumentation), the M.Eng. and Ph.D. degrees in electrical engineering from Universiti Teknologi Malaysia, in 2003, 2005, and 2013, respectively. In 2006, he joined as a Teaching Staff Member at Universiti Malaysia Perlis (UniMAP), Perlis, Malaysia, where he is currently an Associate Professor and a Director of UniMAP Press. His research interests include process tomography, sensors, and instrumentations.

Nurul Syahirah binti Khalid is a Senior Lecturer at Faculty of Electrical Engineering Technology, Universiti Malaysia Perlis. In the year 2010, she graduated with a Bachelor in Mechatronics Engineering with honours from Universiti Teknikal Malaysia Melaka (UTeM). After that in year 2012, she received her Masters Degree in Electrical (Mechatronics and Automation Control Engineering) from Universiti Teknologi Malaysia (UTM), Skudai, Johor. She received her PhD Degree in Mechatronic Engineering from Faculty of Electrical Engineering, Universiti Malaysia Perlis (UniMAP) in 2020. She is currently active doing researches in the field of data fusion, sensor data fusion, machine learning and control system.

Aimi Salihah Abdul Nasir received her B.Eng (Hons) degree in Mechatronic Engineering from Universiti Malaysia Perlis (UniMAP) in 2009 and M.Sc in Biomedical Electronic Engineering from the same university in 2011. In 2015, she obtained her PhD specialized in medical image processing focusing on the clustering analysis from the same university. Her research interests include image processing, medical image analysis, artificial neural network and medical diagnostic system.

N. A. Ramli received her B. Eng. degree Engineering (Hons) Electronics (Instrumentation), M.Sc. degree in Information Telecommunication & Engineering from Universiti Teknologi MARA, Malaysia, PhD Degree in Mechatronic Engineering from Faculty of Electrical Engineering, Universiti Malaysia Perlis (UniMAP) in 2013, 2016 and 2023 respectively. Her research interests, including radio tomography and RF communication system.